Supporting information

Hydroxy and surface oxygen effects on 5−hydroxymethylfurfural oxidation to 2,5−furandicarboxylic acid on β-MnO_2: DFT, microkinetic and experiment studies

Bunrat Tharat,[a] Lappawat Ngamwongwan,[a] Theerada Seehamongkol,[b] Bunyarat Rungtaweevoranit,[b] Jeeranan Nonkumwong,[b] Suwit Suthirakun,[a*] Kajornsak Faungnawakij,[b*] Narong Chanlek,[c] Aunyamanee Plucksacholatarn,[b] Weerawan Nimsaila,[b] Chanatkran Prommin[a] and Anchalee Junkaew[b*]

[a]School of Chemistry, Institute of Science, Suranaree University of Technology, Nakhon Ratchasima, Thailand 30000.

[b]National Nanotechnology Center (NANOTEC), National Science and Technology Development Agency (NSTDA), 111 Thailand Science Park, Pathum Thani, Thailand 12120

[c]Synchrotron Light Research Institute (Public Organization), 111 University Avenue, Muang District, Nakhon Ratchasima, 30000, Thailand

*Corresponding authors: E-mail: A. Junkaew: anchalee@nanotec.or.th, S. Suthirakun: suthirak@sut.ac.th, K. Faungnawakij: kajornsak@nanotec.or.th

Table of Contents

S1. DFT calculations and microkinetic modeling

S1.1 Additional DFT computational details

The Mn $3d^6 4s^1$, O $2s^2 2p^4$, C $2s^2 2p^2$, and H $1s^1$ were treated as valence electrons. All gas-phase simulations were calculated in a cubic box of 15×15×15 Å^3. A bulk structure of the rutile-type β-MnO_2 was optimized by the k-point grid of 7×7×11. A 4×2 β-MnO_2(110) slab with dimensions of 11.48 Å× 12.43 Å × 23.09 Å was cleaved from the optimized bulk structure. Three β-MnO_2 layers consisting of 48 Mn atoms and 96 O atoms were separated by 15 Å of vacuum region along the z-axis to avoid interactions between periodic images (Figure S1a, S1b). The bottom layer was fixed to their bulk lattice positions, whereas the two top layers and adsorbed species were allowed to fully relax during the calculations. The possible active sites of the β-MnO_2(110) slab are atop site of four-fold-coordinate Mn (top-Mn_{4c}), atop site of five-fold-coordinate (top-Mn_{5c}), bridge site between two four-fold-coordinate Mn atoms (bridge-Mn_{4c}), and atop site of three-fold-coordinate O (top-O_{3c}) as presented in Figure S1c.

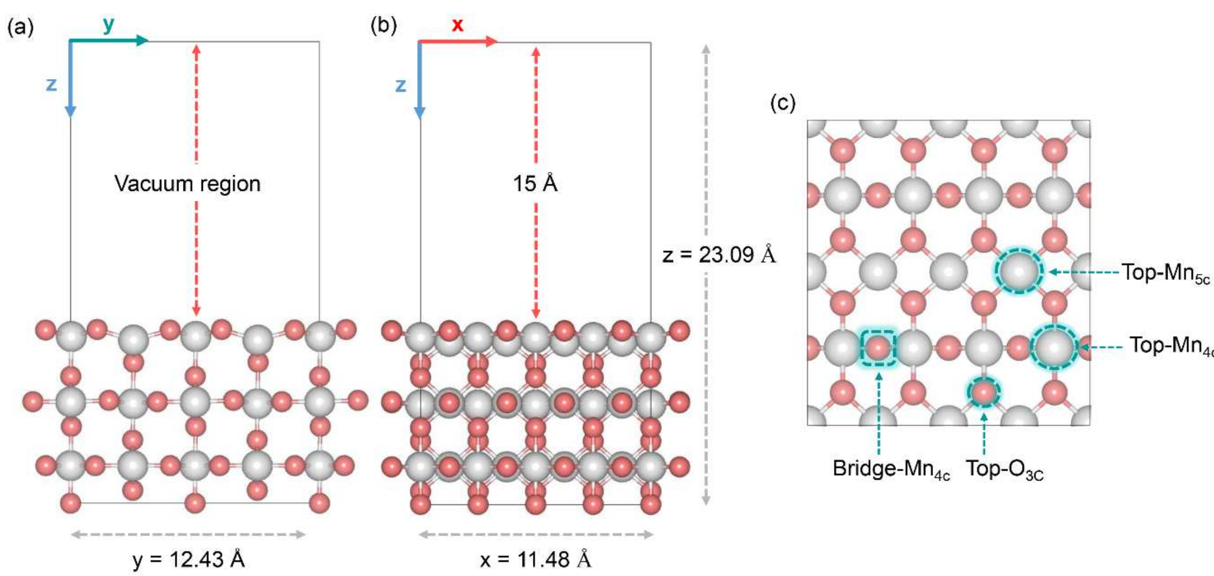

Figure S1. Structure of the β-MnO_2(110) slab projected along (a) the (010) direction (b) (100) the direction, and (c) possible active sites on the β-MnO_2(110) surface.

The zero-point energy and the vibrational partition functions are calculated as,

$$E_{ZPE} = \sum_i \frac{h\nu_i}{2}$$

$$q_{vib} = \prod_i \frac{1}{1 - e^{-h\nu_i/k_B T}}$$

where ν_i is the vibrational frequency of each vibrational mode of the adsorbed species that are calculated from the DFT.

S1.2 HMF adsorption on β-MnO_2(110) surface

The possible adsorption modes of HMF on the β-MnO_2(110) surface were carried out in this part. The HMF molecule possibly attaches the oxygen of hydroxyl group and/or the oxygen of formyl group with the surface forming a bridge-like configuration or end-on configurations as illustrated in Figure S2.

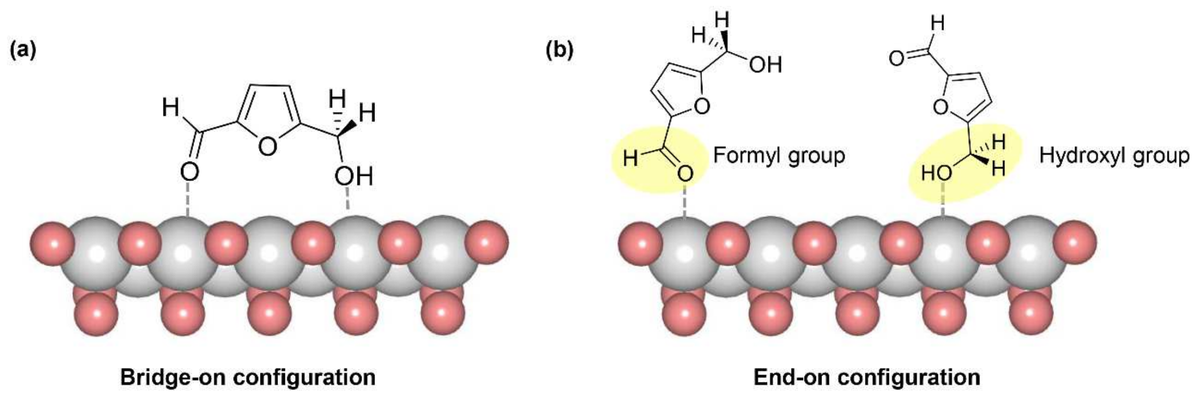

Figure S2. The HMF adsorption modes on the β–MnO_2(110) surface (a) bridge-on configuration, and (b) end-on configurations.

The adsorption energy (E_{ads}) of HMF molecule on β-MnO_2(110) surface was calculated as follows:

$$E_{ads} = E_{HMF/MnO2} - E_{MnO2} - E_{HMF}$$

where $E_{HMF/MnO2}$ is the total energy of the adsorbate molecule-substrate complex, E_{MnO2} is the total energy of a bare β-MnO_2(110) surface, and E_{HMF} is the total energy of an isolated HMF molecule in a vacuum. A negative E_{ads} indicates energetically favorable adsorption.

The calculated adsorption energy (E_{ads}) and bond lengths between selected atoms of HMF molecule and β–MnO_2(110) surface are summarized in Table S1. Figure S3 shows the relevant adsorption configurations. Due to the unsaturated coordination of Mn_{4c} sites enable them to act as active sites assisting the nucleophilic attack from both functional groups of HMF in the oxidation process. The formyl and hydroxyl groups of HMF molecule interact with the bridge-Mn_{4c} site.

Table S1.1. The calculated E_{ads} (in eV), and bond distances (in Å) of selected atoms of the selected configurations of HMF adsorption on β-MnO_2(110)

Adsorption modes	Configurations	Favored sites	ΔE_{ads} (eV)	$O_{(OH)}$ – Mn_{4C} (Å)	$O_{(c=o)}$ – Mn_{4C} (Å)	$H_{(OH)}$– O (Å)
Formyl-End-on	1A	top-Mn_{4C}	−0.13	–	2.02	–
Hydroxyl-End-on	1B	bridge-Mn_{4C}	−0.82	2.20, 2.33	–	2.36, 2.47
Vertical-Bridge-on	1C	bridge-Mn_{4C}	−0.34	2.26, 2.34	2.13, 2.91	2.22, 2.29
	1D	bridge-Mn_{4C}	−1.44	2.24, 3.26	2.19, 2.33	2.24
Parallel-Bridge-on	2D	bridge-Mn_{4C}	−1.25	2.29, 2.31	2.26, 2.83	1.94
	3D	top-Mn_{4C}/bridge-Mn4C	−1.14	2.30	2.32, 2.59	2.46

The HMF molecule points oxygen atoms of hydroxyl toward the Mn_{4c} site and formyl groups toward the on-bridge site called a 1D parallel configuration (see Figure S3). The most stable is the 1D configuration with an adsorption energy of −1.44 eV. This indicates chemisorption and quite strong binding of HMF on β−MnO_2(110). Similarly, 2D and 3D parallel configurations show the E_{ads} of −1.25 eV and −1.14 eV, respectively. The bridge-on configurations are preferable than the end-on configurations, which agrees well with the result of HMF adsorption on β−MnO_2(110) reported previously.[1] The calculated E_{ads} in this work is similar to the HMF adsorption on Pd/α−MnO_2(110) (−3.34 eV)[2], Pd_{13}/α−MnO_2(110) (−2.79 eV)[2], which are more energetically stable than that of Co_3O_4(110) (−1.56 eV)[1], and CuO(111) (−0.79 eV).[1]

It is to be noted that the 2D configuration was used as the initial structure to study the reaction mechanism of the HMF oxidation to FDCA. Its E_{ads} value is slightly higher than that of the 1D configuration and its structure is more suitable for the oxidation reaction. The hydrogen bond between H of hydroxyl group and the oxygen active site on the surface with the distance of 1.94 Å leading to the O–H bond elongation from 0.97 Å to 0.99 Å.

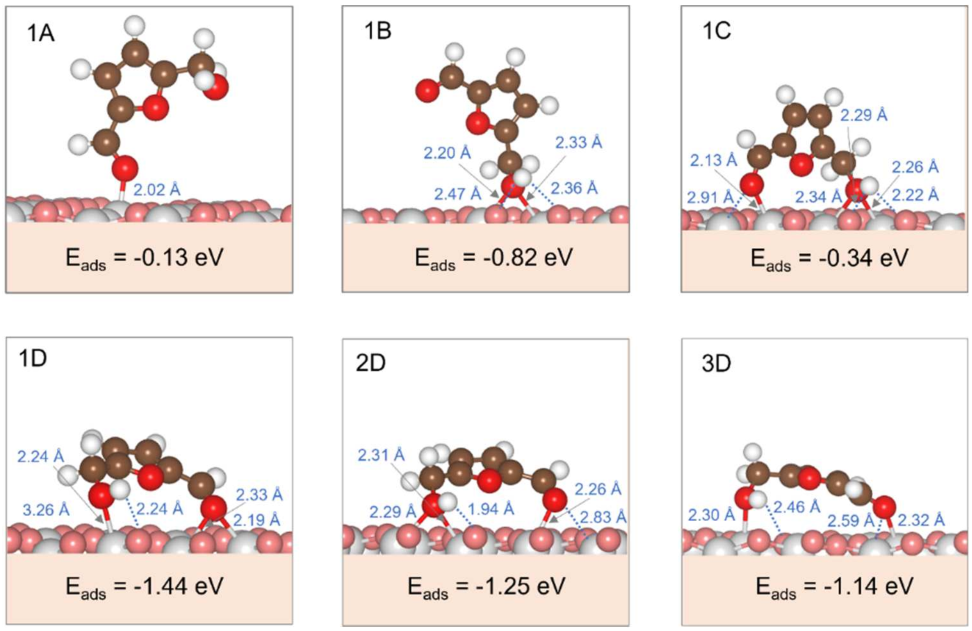

Figure S3. The possible adsorption configurations of HMF on the β-MnO_2(110) surface.

S1.3 Hydroxylation over the β–MnO_2 (110) surface

To understand hydroxylation over the β-MnO_2(110) surface, H_2O adsorption and dissociation in different coverage (θ) are investigated in this part. As shown in Figure S4a and b, the E_{ads} increases (or less stability) when the coverage increases. The result also suggests that the OH coverage of 0.13 is the most thermodynamically stable configuration due to its lowest free energy compared to others, as shown in Figure S4b and S4c. Figure S4c and S4d reveal the free energy increases when the temperature increases. The partial hydroxylation over the β-MnO_2(110) surface occurs at the temperature, 393 K, used in our experiment.

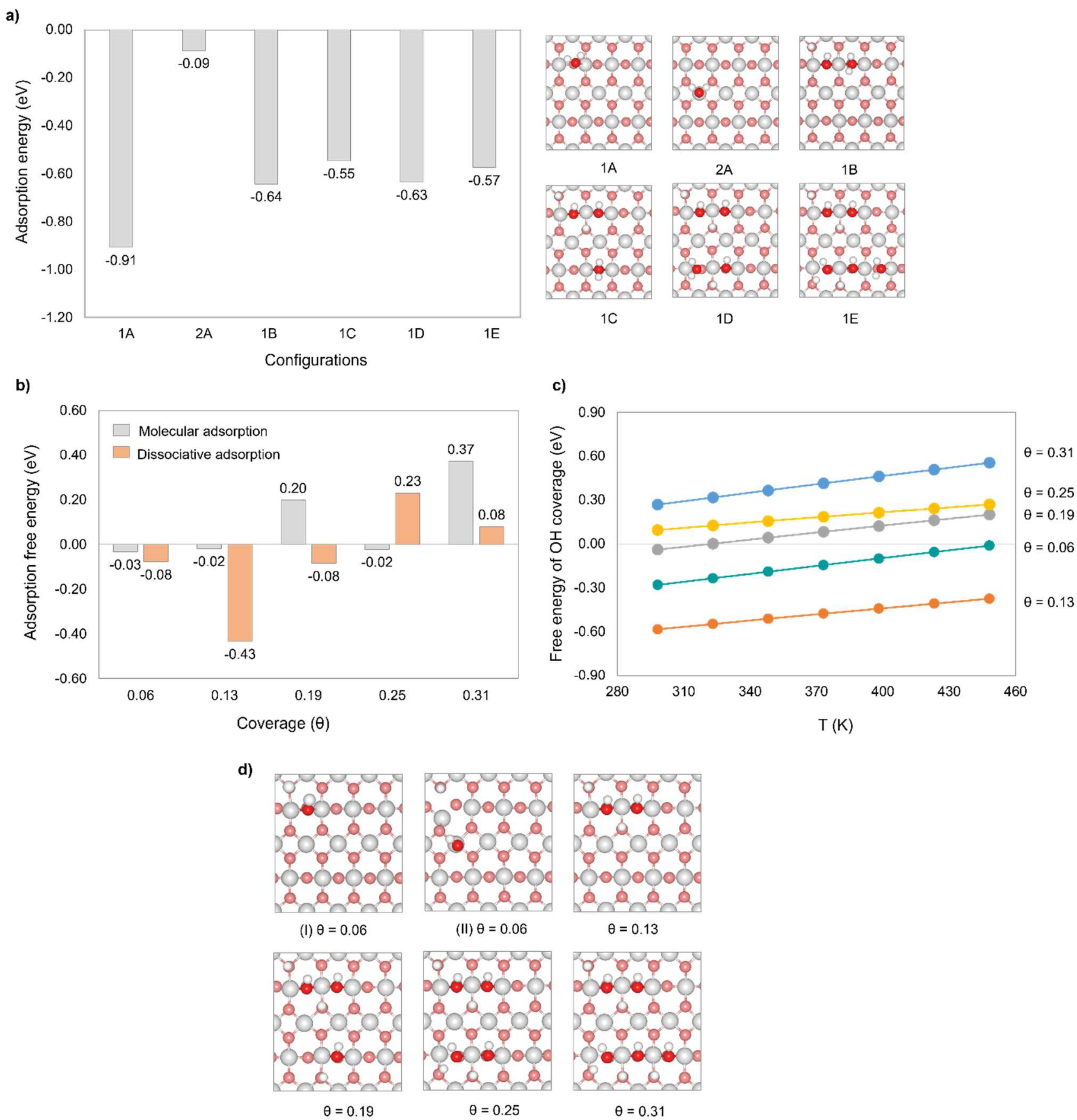

Figure S4. (a) Adsorption energy (E_{ads}) of H_2O on the bare-surfaces (1A and 2A) and hydroxylated surfaces (1B, 1C, 1D, and 1E). (b) Adsorption free energy (G_{ads}) of molecular and dissociated H_2O over β−MnO_2 at 393 K. (c) Free energy of OH coverage on β−MnO_2 versus temperature (T) and (d) the most stable structure of each OH coverage model.

S1.4 Oxygen vacancy formation energy on β−MnO_2 (110) surface

Active surface oxygen is essential in the HMF oxidation if the catalyst surface has low hydroxyl group coverage. We found that the C-H bond breaking of acetal and hemiacetal-like structures has an oxygen vacancy (V_O*) formation simultaneously occurring on the surface (R3, R10, R14, and R21). The low oxygen vacancy formation energy results in a strong oxidizing ability and facilitates the detachment of oxygen atoms from the surface of the catalyst. Therefore, we have calculated the oxygen vacancy formation energy on the bare and hydroxylated surface. The energy of oxygen vacancy formation, E_{VO}, can be calculated from the following equation.

$$E_{VO} = E_{O-vacancy} + \frac{1}{2}E_{O_2} - E_{perfect}$$

where $E_{O\text{-}vacancy}$ and $E_{perfect}$ are the calculated total energies of the surface with one oxygen vacancy and the perfect surface, respectively. E_{O_2} is the total energy of an isolated O_2 molecule.

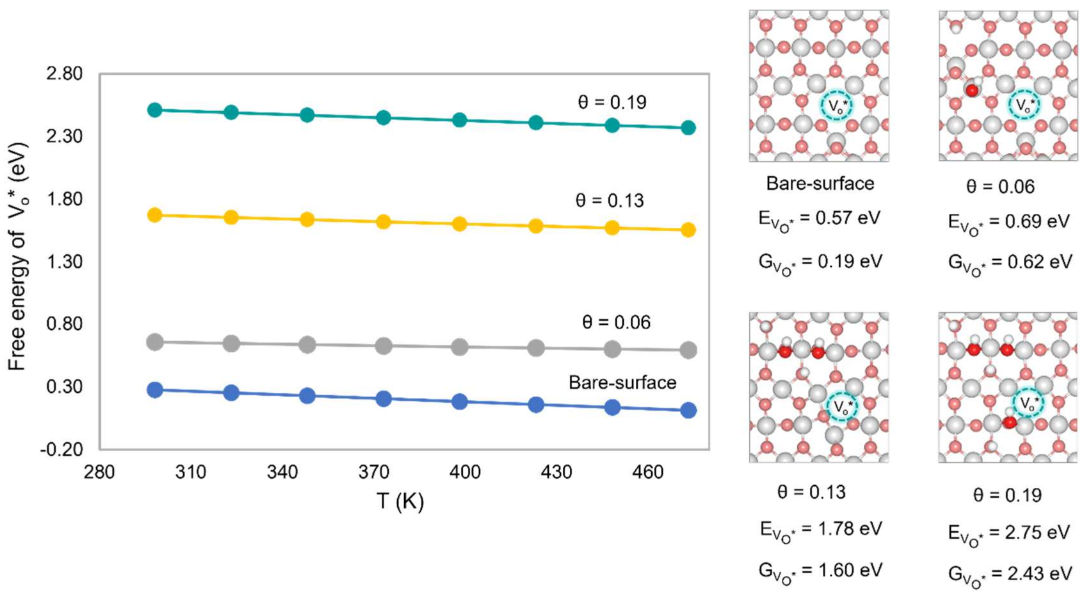

Figure S5. Free energy of oxygen vacancy formation (G_{VO}*) versus temperature (T) and the most stable structure of each vacancy formation model on bare- and hydroxylated β−MnO_2 (110) surfaces (G_{VO}* at 393 K).

The result reveals that the oxygen vacancy formation energy on a bare surface (G_{VO*} = 0.19 eV) is lower than on a hydroxylated surface. Increasing OH coverage on the surface (0.06 to 0.19) leads to the increase of V_O* energy. Moreover, the free energy of V_O* slightly decreases at elevated temperatures, as shown in Figure S5. This result indicates oxygen vacancy formation on the bare surface is easier than that on a hydroxylated surface. As shown in Table 1, the C-H bond breaking of hemiacetal-like structure at TSC4 ($\Delta G^{\neq}$=1.01 eV) via R21 has an energy barrier higher than the TSC2 ($\Delta G^{\neq}$=0.67 eV) via R14. TSC4 of pathway CI-OH associates surface oxygen formation near the OH site resulting in the higher $\Delta G^{\neq}$ value than TSC2 of pathway C, that the surface oxygen formation is easier.

S1.5 Energy profiles of HMF oxidation

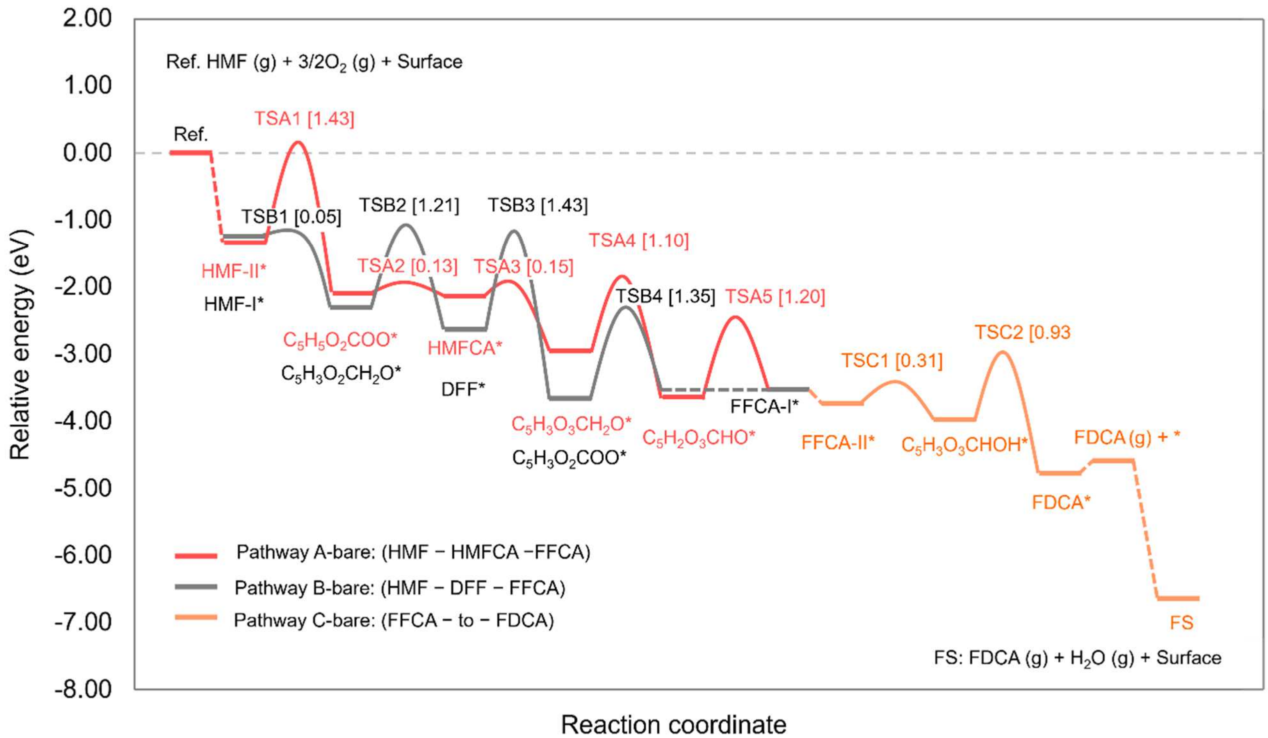

Figure S6. Energy profile of HMF oxidation on bare β-MnO_2(110) surface.

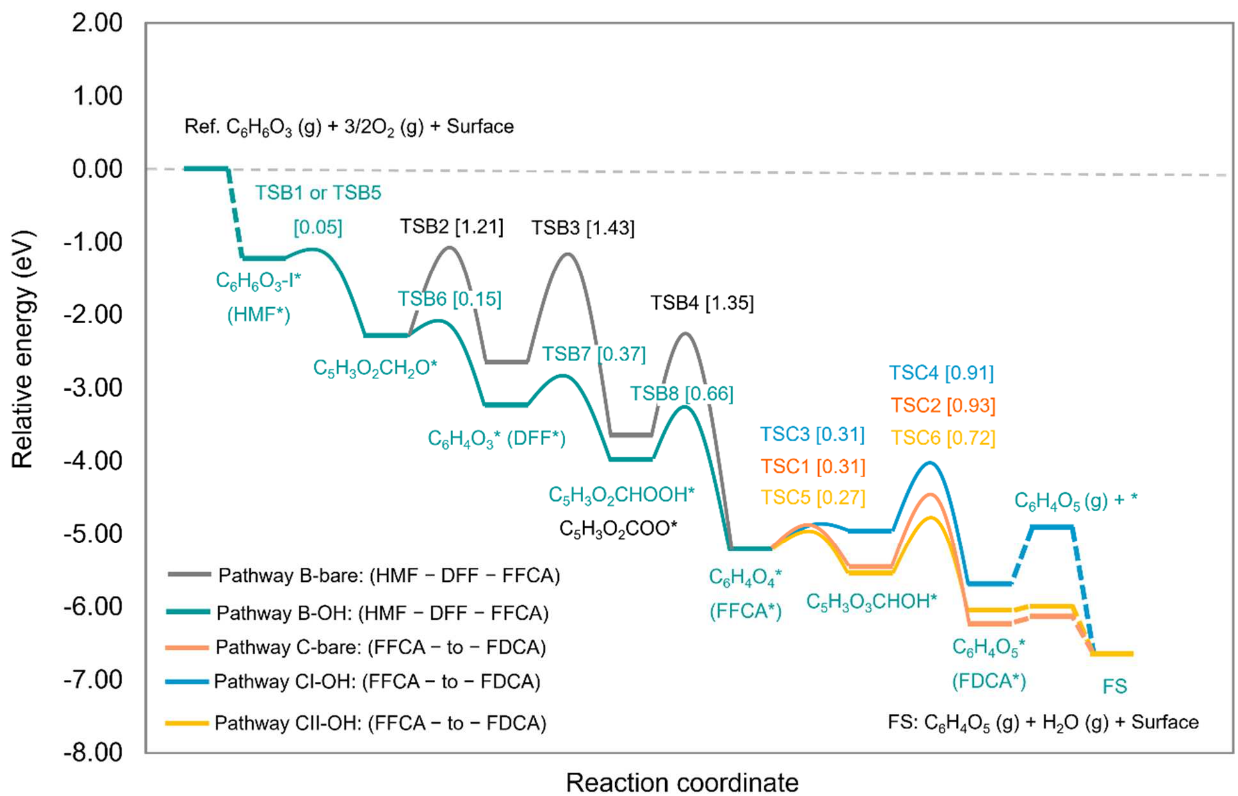

Figure S7. Comparison of energy profiles of HMF oxidation on bare- and hydroxylated surfaces.

Table S1.2. The calculated energy barrier (E_a) and reaction energy (ΔE) at 0K for each elementary step of HMF oxidation on bare and hydroxylated β-MnO_2(110) surfaces.

Reaction step	Elementary step	E_a (eV)	ΔE (eV)
R1	$C_6H_6O_3(g) + * \rightleftharpoons C_6H_6O_3\text{-I}^*$		-1.25
Pathway A-bare			
R2	$C_6H_6O_3\text{-I}^* \rightleftharpoons C_6H_6O_3\text{-II}^*$		-0.06
R3	$C_6H_6O_3\text{-II}^* + O^* \rightleftharpoons C_5H_5O_2COO^* + H^* + V_O^*$	1.43	-0.79
R4	$C_5H_5O_2COO^* + H^* \rightleftharpoons C_6H_6O_4^*$	0.13	-0.05
R5	$C_6H_6O_4^* \rightleftharpoons C_5H_3O_3CH_2O^* + H^*$	0.15	-0.81
R6	$C_5H_3O_3CH_2O^* \rightleftharpoons C_5H_2O_3CHO^* + 2H^*$	1.10	-0.69
R7	$C_5H_2O_3CHO^* + H^* \rightleftharpoons C_6H_4O_4\text{ -I}^*$	1.20	0.15
Pathway B-bare			
R8	$C_6H_6O_3\text{-I}^* \rightleftharpoons C_5H_3O_2CH_2O^* + H^*$	0.05	-1.06
R9	$C_5H_3O_2CH_2O^* \rightleftharpoons C_6H_4O_3^* + H^*$	1.21	-0.33
R10	$C_6H_4O_3^* + O^* \rightleftharpoons C_5H_3O_2COO^* + H^* + V_{O*}$	1.43	-1.03
R11	$C_5H_3O_2COO^* + H^* \rightleftharpoons C_6H_4O_4\text{ -I}^*$	1.35	0.16
Pathway C-bare			
R12	$C_6H_4O_4\text{ -I}^* \rightleftharpoons C_6H_4O_4\text{ -II}^*$		-0.24
R13	$C_6H_4O_4\text{ -II}^* + H^* \rightleftharpoons C_5H_3O_3CHOH^*$	0.31	-0.22
R14	$C_5H_3O_3CHOH^* + O^* \rightleftharpoons C_6H_4O_5^* + V_{O*}$	0.93	-0.79
R15	$C_6H_4O_5^* \rightleftharpoons C_6H_4O_5\text{ (g)} + *$		0.12
Pathway B-OH			
R16 (or R8)	$C_6H_6O_3\text{-I}^* \rightleftharpoons C_5H_3O_2CH_2O^* + H^*$	0.05	-1.06
R17	$C_5H_3O_2CH_2O^* + {}^*OH \rightleftharpoons C_6H_4O_3* + H_2O^*$	0.15	-0.94
R18	$C_6H_4O_3* + {}^*OH \rightleftharpoons C_5H_3O_2CHOOH^*$	0.37	-0.74
R19	$C_5H_3O_2CHOOH^* + {}^*OH \rightleftharpoons C_6H_4O_4^* + H_2O^*$	0.66	-1.24
Pathway CI-OH			
R20 (or R13)	$C_6H_4O_4^* + H^* \rightleftharpoons C_5H_3O_3CHOH^*$	0.31	0.27
R21	$C_5H_3O_3CHOH^* + {}^*OH + O^* \rightleftharpoons C_6H_4O_5^* + H_2O^* + V_O*$	0.91	-0.76
R22	$C_6H_4O_5^* + H_2O^* \rightleftharpoons C_6H_4O_5\text{ (g)} + * + H_2O^*$		0.78
Pathway CII-OH			
R23	$C_6H_4O_4^* + {}^*OH \rightleftharpoons C_5H_3O_3CHOOH^*$	0.27	-0.29
R24	$C_5H_3O_3CHOOH^* + {}^*OH \rightleftharpoons C_6H_4O_5^* + H_2O^*$	0.72	-0.53
R25	$C_6H_4O_5^* + H_2O^* \rightleftharpoons C_6H_4O_5\text{ (g)} + * + H_2O^*$		0.02

S1.6 Microkinetic modeling

Table S2. The elementary steps and the rate equations of HMF oxidation on the β-MnO_2(110) surface used in the microkinetic modelling, which is equivalent to the elementary steps in Table 1.

Reaction step	Elementary step	Rate equations
R1	$C_6H_6O_3(g) + * \rightleftharpoons C_6H_6O_3\text{-I}^*$	$r_1 = k_1 P_{C_6H_6O_3}\theta_* - k_{-1}\theta_{C_6H_6O_3-I}$
Pathway A-bare		
R2	$C_6H_6O_3\text{-I}^* \rightleftharpoons C_6H_6O_3\text{-II}^*$	$r_2 = k_2\theta_{C_6H_6O_3-I} - k_{-2}\theta_{C_6H_6O_3-II}$
R3	$C_6H_6O_3\text{-II}^* \rightleftharpoons C_5H_5O_2COO\_H\_V_O{}^*$	$r_3 = k_3\theta_{C_6H_6O_3-II} - k_{-3}\theta_{C_5H_5O_2COO\_H\_V_O}$
R4	$C_5H_5O_2COO\_V_O\_H{}^* \rightleftharpoons C_6H_6O_4\_V_O{}^*$	$r_4 = k_4\theta_{C_5H_5O_2COO\_H\_V_O} - k_{-4}\theta_{C_6H_6O_4\_V_O}$
R5	$C_6H_6O_4\_V_O{}^* \rightleftharpoons C_5H_3O_3CH_2O\_H\_V_O{}^*$	$r_5 = k_5\theta_{C_6H_6O_4\_V_O} - k_{-5}\theta_{C_5H_3O_3CH_2O\_H\_V_O}$
R6	$C_5H_3O_3CH_2O\_H\_V_O{}^* \rightleftharpoons C_5H_2O_3CHO\_3H\_V_O{}^*$	$r_6 = k_6\theta_{C_5H_3O_3CH_2O\_H\_V_O} - k_{-6}\theta_{C_5H_2O_3CHO\_3H\_V_O}$
R7	$C_5H_2O_3CHO\_3H\_V_O{}^* \rightleftharpoons C_6H_4O_4\_2H\_V_O\text{-I}^*$	$r_7 = k_7\theta_{C_5H_2O_3CHO\_3H\_V_O} - k_{-7}\theta_{C_6H_4O_4\_2H\_V_O-I}$
R7′	$C_5H_2O_3CHO\_3H\_V_O{}^* \rightleftharpoons C_6H_4O_4\_2H\_V_O\text{-II}^*$	$r_{7'} = k_{7'}\theta_{C_5H_2O_3CHO\_3H\_V_O} - k_{-7'}\theta_{C_6H_4O_4\_2H\_V_O-II}$
Pathway B-bare		
R8	$C_6H_6O_3\text{-I}^* \rightleftharpoons C_5H_3O_2CH_2O\_H^*$	$r_8 = k_8\theta_{C_6H_6O_3-I} - k_{-8}\theta_{C_5H_3O_2CH_2O\_H}$
R9	$C_5H_3O_2CH_2O\_H^* \rightleftharpoons C_6H_4O_3\_2H^*$	$r_9 = k_9\theta_{C_5H_3O_2CH_2O\_H} - k_{-9}\theta_{C_6H_4O_3\_2H}$
R10	$C_6H_4O_3\_2H^* \rightleftharpoons C_5H_3O_2COO\_3H\_V_O{}^*$	$r_{10} = k_{10}\theta_{C_6H_4O_3\_2H} - k_{-10}\theta_{C_5H_3O_2COO\_3H\_V_O}$
R11	$C_5H_3O_2COO\_3H\_V_O{}^* \rightleftharpoons C_6H_4O_4\_2H\_V_O\text{-I}^*$	$r_{11} = k_{11}\theta_{C_5H_3O_2COO\_3H\_V_O} - k_{-11}\theta_{C_6H_4O_4\_2H\_V_O-I}$
Pathway C-bare		
R12	$C_6H_4O_4\_2H\_V_O\text{-I}^* \rightleftharpoons C_6H_4O_4\_2H\_V_O\text{-II}^*$	$r_{12} = k_{12}\theta_{C_6H_4O_4\_2H\_V_O-I} - k_{-12}\theta_{C_6H_4O_4\_2H\_V_O-II}$

R13	$C_6H_4O_4\_2H\_V_O\text{-}II^* \rightleftharpoons C_5H_3O_3CHOH\_H\_V_O^*$	$r_{13} = k_{13}\theta_{C_6H_4O_4\_2H\_V_O-II} - k_{-13}\theta_{C_5H_3O_3CHOH\_H\_V_O}$
R14	$C_5H_3O_3CHOH\_H\_V_O^* \rightleftharpoons C_6H_4O_5\_2H\_2V_O^*$	$r_{14} = k_{14}\theta_{C_5H_3O_3CHOH\_H\_V_O} - k_{-14}\theta_{C_6H_4O_5\_2H\_2V_O}$
R15	$C_6H_4O_5\_2H\_2V_O^* \rightleftharpoons C_6H_4O_5(g) + {}^*2H\_2V_O$	$r_{15} = k_{15}\theta_{C_6H_4O_5\_2H\_2V_O} - k_{-15}P_{C_6H_4O_5}\theta_{2H\_2V_O}$
Pathway B-OH		
R16 (or R8)	$C_6H_6O_3\text{-}I^* \rightleftharpoons C_5H_3O_2CH_2O\_H^*$	$r_{16} = k_{16}\theta_{C_6H_6O_3-I} - k_{-16}\theta_{C_5H_3O_2CH_2O\_H}$
R17	$C_5H_3O_2CH_2O\_H^* + H_2O(g) \rightleftharpoons C_5H_3O_2CH_2O\_2H\_OH^*$	$r_{17} = k_{17}\theta_{C_5H_3O_2CH_2O\_H}P_{H_2O} - k_{-17}\theta_{C_5H_3O_2CH_2O\_2H\_OH}$
R17′	$C_5H_3O_2CH_2O\_2H\_OH^* \rightleftharpoons C_6H_4O_3\_2H\_H_2O^*$	$r_{17'} = k_{17'}\theta_{C_5H_3O_2CH_2O\_2H\_OH} - k_{-17'}\theta_{C_6H_4O_3\_2H\_H_2O}$
R18	$C_6H_4O_3\_2H\_H_2O^* \rightleftharpoons C_6H_4O_3\_3H\_OH^*$	$r_{18} = k_{18}\theta_{C_6H_4O_3\_2H\_H_2O} - k_{-18}\theta_{C_6H_4O_3\_3H\_OH}$
R18′	$C_6H_4O_3\_3H\_OH^* \rightleftharpoons C_5H_3O_2CHOOH\_3H^*$	$r_{18'} = k_{18'}\theta_{C_6H_4O_3\_3H\_OH} - k_{-18'}\theta_{C_5H_3O_2CHOOH\_3H}$
R19	$C_5H_3O_2CHOOH\_3H^* + H_2O(g) \rightleftharpoons$ $C_5H_3O_2CHOOH\_4H\_OH^*$	$r_{19} = k_{19}\theta_{C_5H_3O_2CHOOH\_3H}P_{H_2O} - k_{-19}\theta_{C_5H_3O_2CHOOO\_4H\_OH}$
R19′	$C_5H_3O_2CHOOH\_4H\_OH^* \rightleftharpoons C_6H_4O_4\_4H\_H_2O^*$	$r_{19'} = k_{19'}\theta_{C_5H_3O_2CHOOO\_4H\_OH} - k_{-19'}\theta_{C_6H_4O_4\_4H\_H_2O}$
R19″	$C_6H_4O_4\_4H\_H_2O^* \rightleftharpoons C_6H_4O_4\_2H\_V_O\text{-}I^* + 2H_2O(g)$	$r_{19''} = k_{19''}\theta_{C_6H_4O_4\_4H\_H_2O} - k_{-19''}\theta_{C_6H_4O_4\_2H\_V_O-II}P_{H_2O}^2$
Pathway CI-OH		
R20 (or R13)	$C_6H_4O_4\_2H\_V_O\text{-}II^* \rightleftharpoons C_5H_3O_3CHOH\_H\_V_O^*$	$r_{20} = k_{20}\theta_{C_6H_4O_4\_2H\_V_O-II} - k_{-20}\theta_{C_5H_3O_3CHOH\_H\_V_O}$
R21	$C_5H_3O_3CHOH\_H\_V_O^* + H_2O(g) \rightleftharpoons$ $C_5H_3O_3CHOH\_2H\_OH\_V_O^*$	$r_{21} = k_{21}\theta_{C_5H_3O_3CHOH\_H\_V_O}P_{H_2O} - k_{-21}\theta_{C_5H_3O_3CHOH\_2H\_OH\_V_O}$
R21′	$C_5H_3O_3CHOH\_2H\_OH\_V_O^* \rightleftharpoons$ $C_6H_4O_5\_2H\_H_2O\_2V_O^*$	$r_{21'} = k_{21'}\theta_{C_5H_3O_3CHOH\_2H\_OH\_V_O} - k_{-21'}\theta_{C_6H_4O_5\_2H\_H_2O\_2V_O}$

R22	$C_6H_4O_5\_2H\_H_2O\_2V_O^*$ ⇌ $C_6H_4O_5$ (g) + $^*2H\_H_2O\_2V_O$	$r_{22} = k_{22}\theta_{C_6H_4O_5\_2H\_H_2O\_2V_O} - k_{-22}P_{C_6H_4O_5}\theta_{2H\_H_2O\_2V_O}$
Pathway CII-OH		
R23	$C_6H_4O_4\_2H\_V_O\text{-}II^*$ + H_2O(g) ⇌ $C_6H_4O_4\_3H\_OH\_V_O^*$	$r_{23} = k_{23}\theta_{C_6H_4O_4\_2H\_V_O-II}P_{H_2O} - k_{-23}\theta_{C_6H_4O_4\_3H\_OH\_V_O}$
R23′	$C_6H_4O_4\_3H\_OH\_V_O^*$ ⇌ $C_5H_3O_3CHOOH\_3H\_V_O^*$	$r_{23'} = k_{23'}\theta_{C_6H_4O_4\_3H\_OH\_V_O} - k_{-23'}\theta_{C_5H_3O_3CHOOH\_3H\_V_O}$
R24	$C_5H_3O_3CHOOH\_3H\_V_O^*$ + H_2O (g) ⇌ $C_5H_3O_3CHOOH\_4H\_OH\_V_O^*$	$r_{24} = k_{24}\theta_{C_5H_3O_3CHOOH\_3H\_V_O}P_{H_2O} - k_{-24}\theta_{C_5H_3O_3CHOOH\_4H\_OH\_V_O}$
R24′	$C_5H_3O_3CHOOH\_4H\_OH\_V_O^*$ ⇌ $C_6H_4O_5\_4H\_H_2O\_V_O^*$	$r_{24'} = k_{24'}\theta_{C_5H_3O_3CHOOH\_4H\_OH\_V_O} - k_{-24'}\theta_{C_6H_4O_5\_4H\_H_2O\_V_O}$
R25	$C_6H_4O_5\_4H\_H_2O\_V_O^*$ ⇌ $C_6H_4O_5$ (g) + $^*4H\_H_2O\_V_O$	$r_{25} = k_{25}\theta_{C_6H_4O_5\_4H\_H_2O\_V_O} - k_{-25}P_{C_6H_4O_5}\theta_{4H\_H_2O\_V_O}$
Catalyst replenishment		
R15′	$^*2H\_2V_O$ + (3/2)O_2 (g) ⇌ H_2O (g) + *	$r_{15'} = k_{15'}\theta_{2H\_2V_O}P_{O_2}^{3/2} - k_{-15'}\theta_*P_{H_2O}$
R22′	$^*2H\_H_2O\_2V_O$ + (3/2)O_2 (g) ⇌ $2H_2O$ (g) + *	$r_{22'} = k_{22'}\theta_{2H\_H_2O\_2V_O}P_{O_2}^{3/2} - k_{-22'}\theta_*P_{H_2O}^2$
R25′	$^*4H\_H_2O\_V_O$ + (3/2)O_2 (g) ⇌ $3H_2O$ (g) + *	$r_{25'} = k_{25'}\theta_{4H\_H_2O\_V_O}P_{O_2}^{3/2} - k_{-25'}\theta_*P_{H_2O}^3$

Note: the rate constants for water adsorption, dissociation and catalyst replenishment are assumed to be fast and not interfere with the calculated overall rate of reaction.

Table S3. The constructed ODE equations for each elementary step of HMF oxidation to FDCA in four microkinetic models including MKM-I, MKM-II, MKM-III, and MKM-IV.

MKM-I	MKM-II
$\frac{d\theta_{C_6H_6O_3-I^*}}{dt} = r_1 - r_2 - r_8$	$\frac{d\theta_{C_6H_6O_3-I^*}}{dt} = r_1 - r_2 - r_{16}$
$\frac{d\theta_{C_6H_6O_3-II^*}}{dt} = r_2 - r_3$	$\frac{d\theta_{C_6H_6O_3-II^*}}{dt} = r_2 - r_3$
$\frac{d\theta_{C_5H_5O_2COO\_H\_V_O*}}{dt} = r_3 - r_4$	$\frac{d\theta_{C_5H_5O_2COO\_H\_V_O*}}{dt} = r_3 - r_4$
$\frac{d\theta_{C_6H_6O_4\_V_O*}}{dt} = r_4 - r_5$	$\frac{d\theta_{C_6H_6O_4\_V_O*}}{dt} = r_4 - r_5$
$\frac{d\theta_{C_5H_3O_3CH_2O\_H\_V_O*}}{dt} = r_5 - r_6$	$\frac{d\theta_{C_5H_3O_3CH_2O\_H\_V_O*}}{dt} = r_5 - r_6$
$\frac{d\theta_{C_5H_3O_3CHO\_3H\_V_O*}}{dt} = r_6 - r_7$	$\frac{d\theta_{C_5H_3O_3CHO\_3H\_V_O*}}{dt} = r_6 - r_7$
$\frac{d\theta_{C_6H_4O_4\_2H\_V_O-I^*}}{dt} = r_7 + r_{11} - r_{12}$	$\frac{d\theta_{C_5H_3O_2CH_2O\_H^*}}{dt} = r_{16} - r_{17}$
$\frac{d\theta_{C_5H_3O_2CH_2O\_H^*}}{dt} = r_8 - r_9$	$\frac{d\theta_{C_5H_3O_2CH_2O\_2H\_OH^*}}{dt} = r_{17} - r_{17'}$
$\frac{d\theta_{C_6H_4O_3\_2H^*}}{dt} = r_9 - r_{10}$	$\frac{d\theta_{C_6H_4O_3\_2H\_H_2O^*}}{dt} = r_{17'} - r_{18}$
$\frac{d\theta_{C_5H_3O_2COO\_3H\_V_O*}}{dt} = r_{10} - r_{11}$	$\frac{d\theta_{C_6H_4O_3\_3H\_OH^*}}{dt} = r_{18} - r_{18'}$
$\frac{d\theta_{C_6H_4O_4\_2H\_V_O-II^*}}{dt} = r_{12} - r_{13}$	$\frac{d\theta_{C_5H_3O_2CHOOH\_3H^*}}{dt} = r_{18'} - r_{19}$
$\frac{d\theta_{C_5H_3O_3CHOH\_H\_V_O*}}{dt} = r_{13} - r_{14}$	$\frac{d\theta_{C_5H_3O_2CHOOO\_4H\_OH^*}}{dt} = r_{19} - r_{19'}$
$\frac{d\theta_{C_6H_4O_5\_2H\_2V_O*}}{dt} = r_{14} - r_{15}$	$\frac{d\theta_{C_6H_4O_4\_4H\_H_2O^*}}{dt} = r_{19'} - r_{19''}$
$\frac{d\theta_{2H\_2V_O*}}{dt} = r_{15} - r_{15'}$	$\frac{d\theta_{C_6H_4O_4\_2H\_V_O-II^*}}{dt} = r_{7'} + r_{19''} - r_{13}$
	$\frac{d\theta_{C_5H_3O_3CHOH\_H\_V_O*}}{dt} = r_{13} - r_{14}$
	$\frac{d\theta_{C_6H_4O_5\_2H\_2V_O*}}{dt} = r_{14} - r_{15}$
	$\frac{d\theta_{2H\_2V_O*}}{dt} = r_{15} - r_{15'}$

MKM-III	MKM-IV
$\frac{d\theta_{C_6H_6O_3-I^*}}{dt} = r_1 - r_2 - r_{16}$	$\frac{d\theta_{C_6H_6O_3-I^*}}{dt} = r_1 - r_2 - r_{16}$
$\frac{d\theta_{C_6H_6O_3-II^*}}{dt} = r_2 - r_3$	$\frac{d\theta_{C_6H_6O_3-II^*}}{dt} = r_2 - r_3$
$\frac{d\theta_{C_5H_5O_2COO\_H\_V_O*}}{dt} = r_3 - r_4$	$\frac{d\theta_{C_5H_5O_2COO\_H\_V_O*}}{dt} = r_3 - r_4$
$\frac{d\theta_{C_6H_6O_4\_V_O*}}{dt} = r_4 - r_5$	$\frac{d\theta_{C_6H_6O_4\_V_O*}}{dt} = r_4 - r_5$
$\frac{d\theta_{C_5H_3O_3CH_2O\_H\_V_O*}}{dt} = r_5 - r_6$	$\frac{d\theta_{C_5H_3O_3CH_2O\_H\_V_O*}}{dt} = r_5 - r_6$
$\frac{d\theta_{C_5H_3O_3CHO\_3H\_V_O*}}{dt} = r_6 - r_7$	$\frac{d\theta_{C_5H_3O_3CHO\_3H\_V_O*}}{dt} = r_6 - r_7$
$\frac{d\theta_{C_5H_3O_2CH_2O\_H^*}}{dt} = r_{16} - r_{17}$	$\frac{d\theta_{C_5H_3O_2CH_2O\_H^*}}{dt} = r_{16} - r_{17}$
$\frac{d\theta_{C_5H_3O_2CH_2O\_2H\_OH^*}}{dt} = r_{17} - r_{17'}$	$\frac{d\theta_{C_5H_3O_2CH_2O\_2H\_OH^*}}{dt} = r_{17} - r_{17'}$
$\frac{d\theta_{C_6H_4O_3\_2H\_H_2O^*}}{dt} = r_{17'} - r_{18}$	$\frac{d\theta_{C_6H_4O_3\_2H\_H_2O^*}}{dt} = r_{17'} - r_{18}$
$\frac{d\theta_{C_6H_4O_3\_3H\_OH^*}}{dt} = r_{18} - r_{18'}$	$\frac{d\theta_{C_6H_4O_3\_3H\_OH^*}}{dt} = r_{18} - r_{18'}$
$\frac{d\theta_{C_5H_3O_2CHOOH\_3H^*}}{dt} = r_{18'} - r_{19}$	$\frac{d\theta_{C_5H_3O_2CHOOH\_3H^*}}{dt} = r_{18'} - r_{19}$
$\frac{d\theta_{C_5H_3O_2CHOOO\_4H\_OH^*}}{dt} = r_{19} - r_{19'}$	$\frac{d\theta_{C_5H_3O_2CHOOO\_4H\_OH^*}}{dt} = r_{19} - r_{19'}$
$\frac{d\theta_{C_6H_4O_4\_4H\_H_2O^*}}{dt} = r_{19'} - r_{19''}$	$\frac{d\theta_{C_6H_4O_4\_4H\_H_2O^*}}{dt} = r_{19'} - r_{19''}$
$\frac{d\theta_{C_6H_4O_4\_2H\_V_O-II^*}}{dt} = r_{7'} + r_{19''} - r_{20}$	$\frac{d\theta_{C_6H_4O_4\_2H\_V_O-II^*}}{dt} = r_{7'} + r_{19''} - r_{23}$
$\frac{d\theta_{C_5H_3O_3CHOH\_H\_V_O*}}{dt} = r_{20} - r_{21}$	$\frac{d\theta_{C_6H_4O_4\_3H\_OH\_V_O*}}{dt} = r_{23} - r_{23'}$
$\frac{d\theta_{C_5H_3O_3CHOH\_2H\_OH\_V_O*}}{dt} = r_{21} - r_{21'}$	$\frac{d\theta_{C_5H_3O_3CHOOH\_3H\_V_O*}}{dt} = r_{23'} - r_{24}$
$\frac{d\theta_{C_6H_4O_5\_2H\_H_2O\_2V_O*}}{dt} = r_{21'} - r_{22}$	$\frac{d\theta_{C_5H_3O_3CHOOH\_4H\_OH\_V_O*}}{dt} = r_{24} - r_{24'}$
$\frac{d\theta_{2H\_H_2O\_2V_O*}}{dt} = r_{22} - r_{22'}$	$\frac{d\theta_{C_6H_4O_4\_3H\_OH\_V_O*}}{dt} = r_{24'} - r_{25}$
	$\frac{d\theta_{4H\_H_2O\_V_O*}}{dt} = r_{25} - r_{25'}$

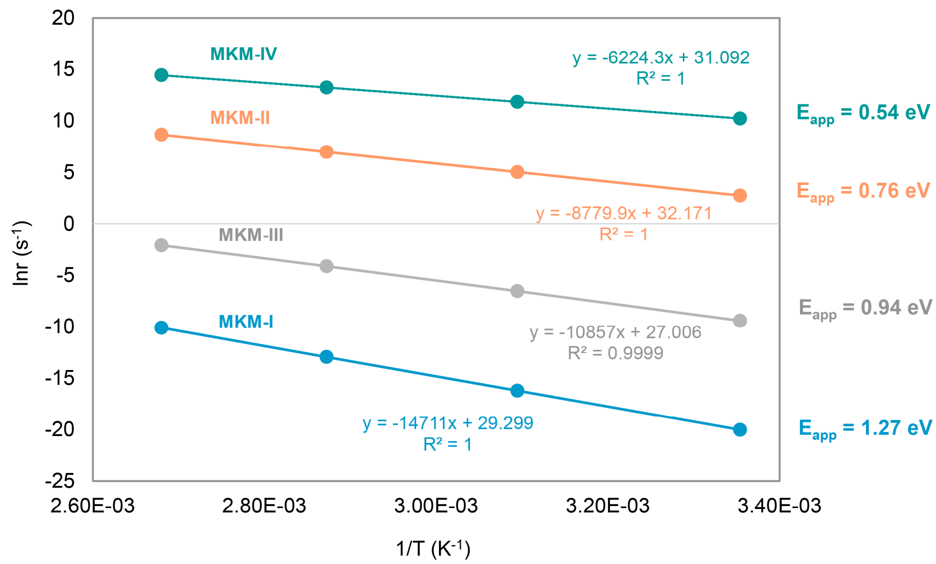

Figure S8. The natural logarithm of reaction rate (in s^{-1}) of HMF oxidation as a function of 1/T (in K^{-1}) and the calculated apparent activation energy (E_{app}) of each microkinetic model.

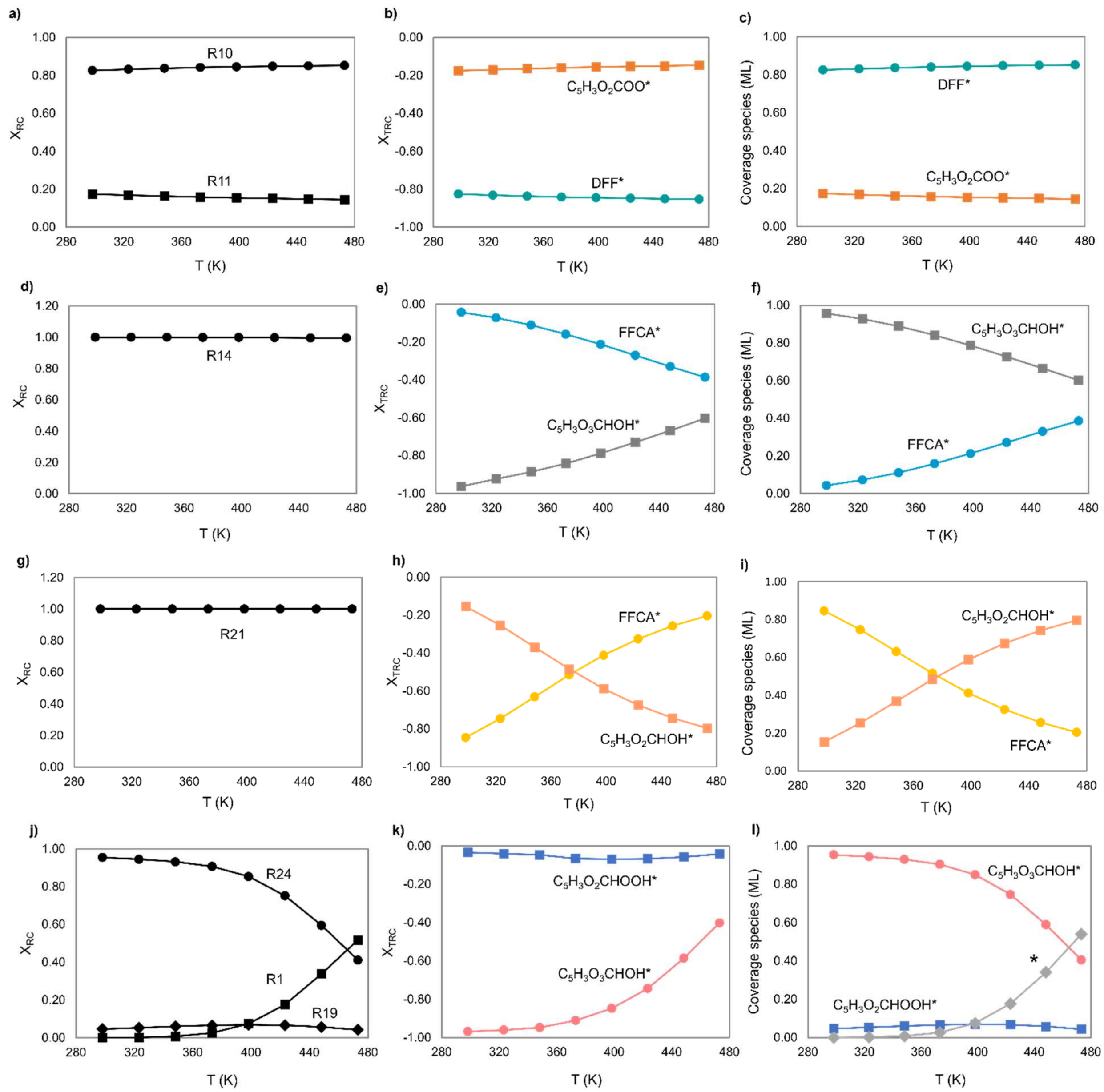

Figure S9. The primary Campbell's degree of rate control ($X_{RC,\,i}$), the degree of thermodynamic rate control ($X_{TRC,\,i}$), and the primary intermediate coverage versus temperature (in K) of HMF oxidation in MKM-I (a, b, and c), MKM-II (d, e, and f), MKM-III (g, h, and i), and MKM-IV (j, k, and l), respectively.

S1.7 Electronic charge analysis

Bader charges[3] of selected configurations were calculated to understand the local charge properties around the active sites as shown in Figure S10. The negative and positive values represent the partial negative charge via electron incretion and the partial positive charge via electron depletion, respectively.

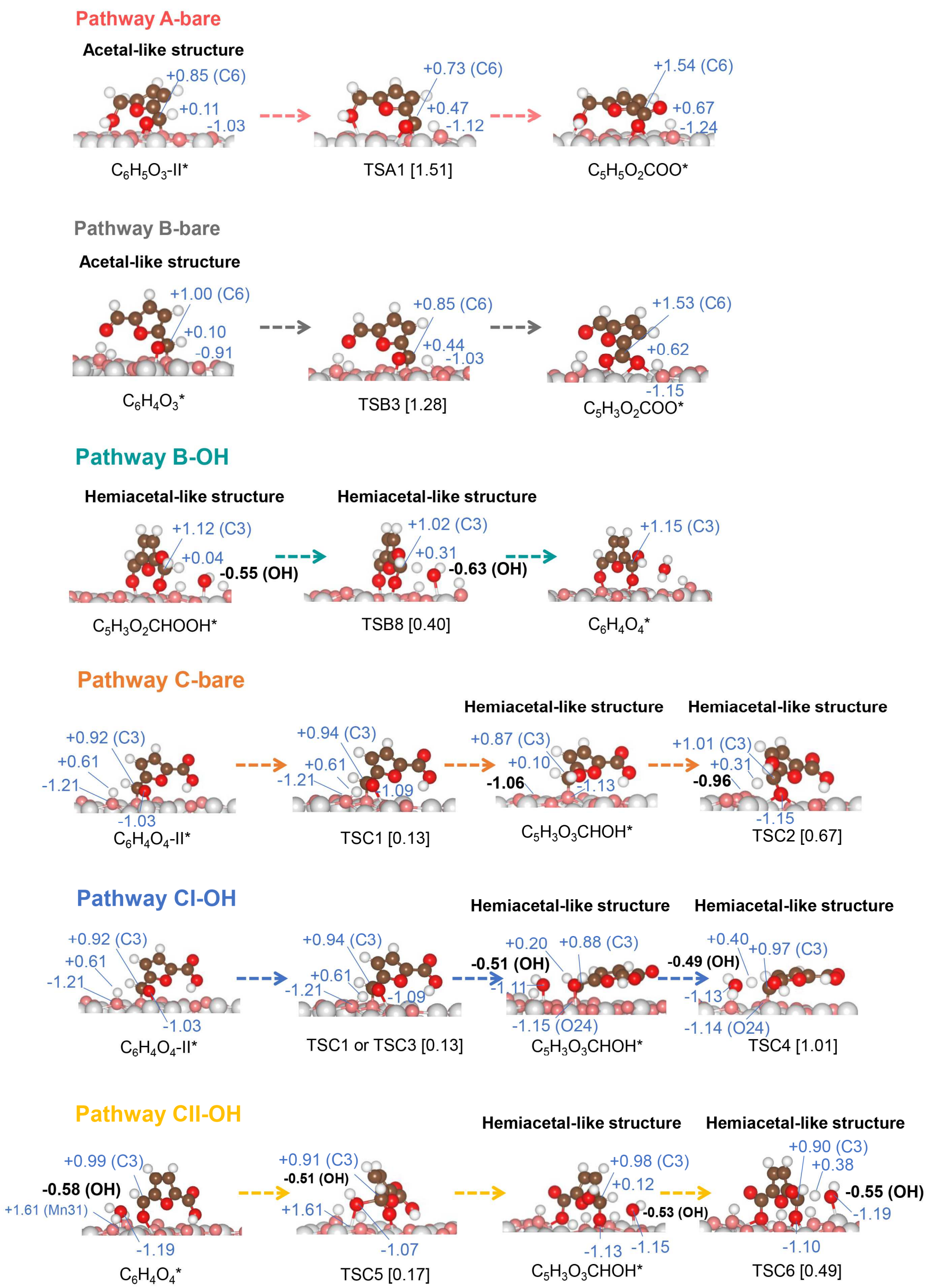

Figure S10. Bader charge analyses of selected steps of HMF oxidation on bare and hydroxylated surfaces. The activation barriers (in eV) are given in square brackets.

S2 Experiment

S2.1 Continuous flow oxidation of HMF over the synthesized β−MnO_2 catalyst

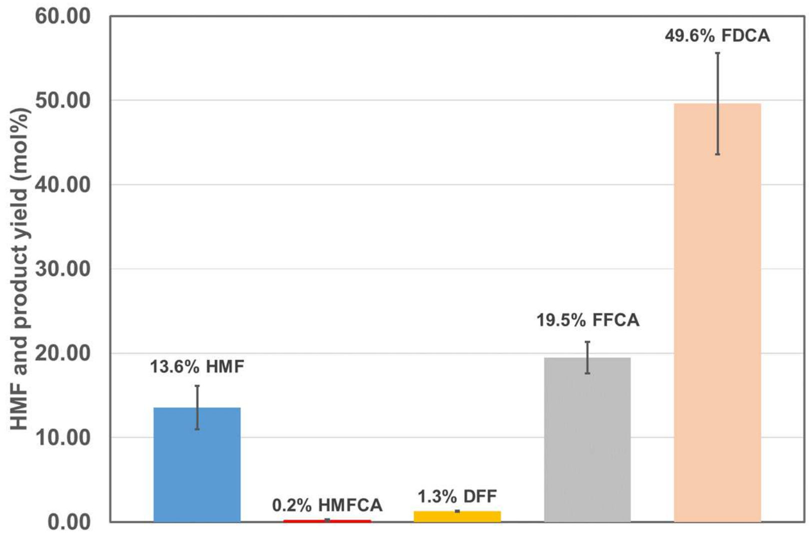

Figure S11. Continuous flow oxidation of HMF over β-MnO_2 catalyst: Reaction conditions: β-MnO_2 (1 mL), HMF in DI water (40 mM), $NaHCO_3$ (3 equiv with respect to HMF), pO_2 (1 MPa), 393 K and LHSV of 4 h^{-1}. Average value over 6-10 h time-on-stream (steady state).

S2.2 Oxidation of HMF using a batch reactor over the synthesized β−MnO_2 catalyst

Experimental procedure. The procedure for catalytic efficiency testing of the obtained β−MnO_2 was adapted from Hayashi et al.[4] The HMF oxidation was carried out in a 100 mL stainless steel autoclave reactor with a 30 mL Teflon liner containing a magnetic stirring bar. Typically, HMF (1.2 mmol), β−MnO_2 powder (300 mg), $NaHCO_3$ (3.6 mmol), water (30 mL), and O_2 (2 MPa) were charged into the autoclave reactor. The reaction solution was heated to 393 K. The solution sampling was started at which the temperature reached set point and collected continually to monitor the progress of reaction. The sampled solution was filtered using 0.22 uM pore size membrane filter and the filtrate was diluted 10 times with water. The formation of FDCA and their intermediates and the decreasing of HMF were investigated using the high performance liquid chromatography (HPLC, Shimadzu), with a UV detector adjusted to 260 nm for analysis of FDCA and HMFCA and to 280 nm for analysis of HMF, FFCA and DFF, using an Aminex HPX-87H ion-exchange column (300 mm in length with a 7.8 mm i.d.; Bio-Rad, Hercules, CA, USA). The column temperature was set at 318 ºC. The samples were eluted with 5 mM sulfuric acid solution in DI water at a flow rate of 0.6 mL/min.

Figure S12 shows the progress of reaction regarding the changes of HMF, HMFCA, DFF, FFCA and FDCA over time. It is seen that DFF and HMFCA intermediates were occurred since 0 hour (i.e., when the temperature reached set point), indicating that reaction pathway from HMF to FFCA occurred through both DFF and HMFCA in the current system. The yields of those intermediates reach their maxima at 4 h for DFF (~3.7%) and 8 h for HMFCA (~3.4%), showing higher rate of DFF production at the beginning. Additionally, DFF which was subsequently oxidized into FFCA are completely consumed before HMFCA, indicating that the pathway with DFF as the intermediate is more dominant than the HMFCA route in the current system. The produced FFCA is gradually increased against reaction time with an increasing of FDCA. After 24 h, the decreasing of FFCA is observed with continuous increasing of FDCA until 45 h at which the FFCA is almost used up whereas the FDCA yield reaches its maximum at ~60%, suggesting that the oxidation of FFCA to FDCA is the rate-determining step.

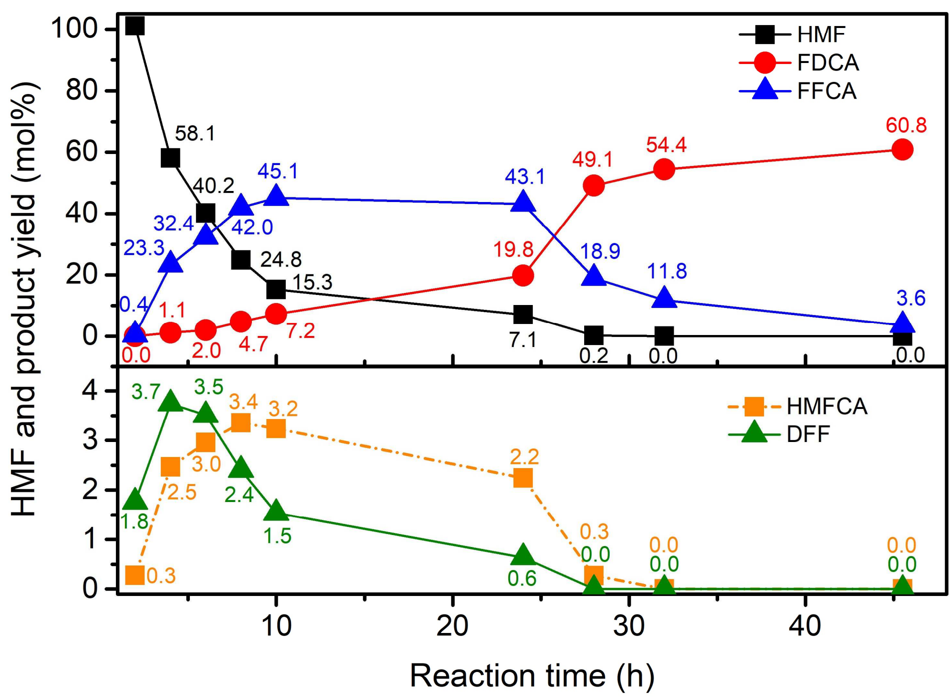

Figure S12. Time course for the oxidation of HMF into FDCA catalyzed by β–MnO_2 in a batch reactor. Reaction conditions: HMF (1.2 mmol), β–MnO_2 powder (300 mg), $NaHCO_3$ (3.6 mmol), water (30 mL), and pO_2 (2 MPa), 393 K.

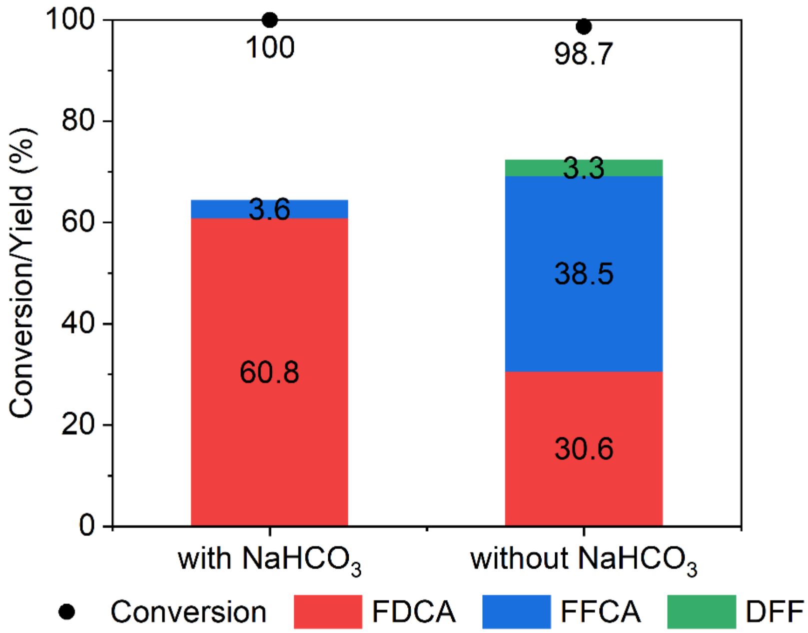

Figure S13. Effects of $NaHCO_3$ on the oxidation of HMF into FDCA catalyzed by β–MnO_2 in a batch reactor. Reaction conditions: HMF (1.2 mmol), β–MnO_2 powder (300 mg), water (30 mL), and pO_2 (2 MPa), 393 K. For the reaction with NaHCO3, $NaHCO_3$ (3.6 mmol) was added to the above reaction mixture prior to heating.

S2.3 Characterizations of the β–MnO_2 catalyst

Temperature-programmed desorption of CO_2 (CO_2 TPD) was carried out using a Dynamic Flow Chemisorption Analyzer equipped with a thermal conductivity detector, Quantachrome Instruments. The catalyst (0.2 g) was pretreated in a He flow (30 mL/min) at 150 °C for 1 h with a ramp rate of 5 °C/min. The catalyst was cooled to 60 °C under He flow (30 mL/min) and CO_2 was then allowed to adsorbed. Finally, the CO_2 TPD experiment was carried out in He flow in a temperature range of 45–800 °C at a ramp rate of 5 °C/min.

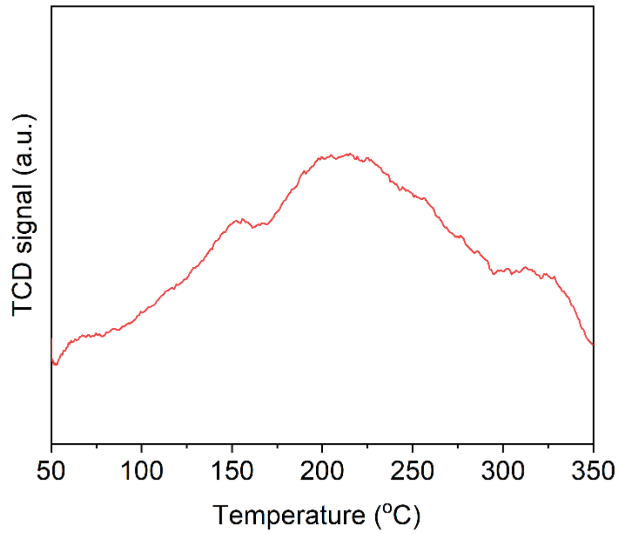

Figure S14. CO_2 TPD of fresh β-MnO_2 catalysts.

In situ DRIFTS was performed using a Nicolet iS50 infrared spectrometer (Thermo Scientific, Waltham, MA, USA) equipped with a mercury-cadmium-telluride (MCT) detector, a diffuse reflection attachment Praying Mantis™ and a high-temperature reaction cell. The catalyst sample was heated to 50 °C under Ar and the spectrum was recorded.

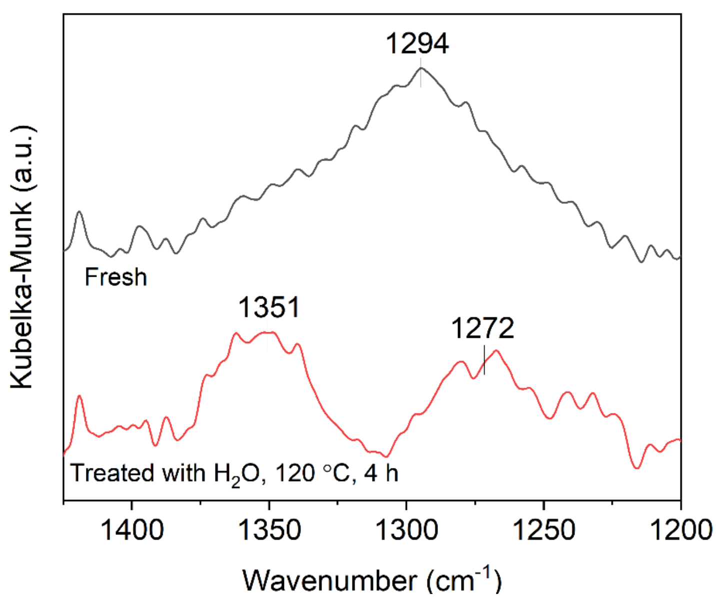

Figure S15. In situ DRIFTS collected at 50 °C under Ar of as synthesized β-MnO_2 catalyst and after treatment with H_2O at 120 °C for 4 h.

S2.4 Characterization of FDCA

A portion of the reaction solution obtained from the flow reactor was acidified using conc. HCl while stirring to precipitate FDCA as shown in Figure S16. Identification of FDCA was further confirmed by ^{1}H and ^{13}C NMR analysis as shown in Figure S17 and S18, respectively. ^{1}H and ^{13}C NMR analyses show that the product is indeed FDCA as the peaks are well correspond to the structure of FDCA.[5]

Figure S16. FDCA obtained from the acidification of reaction solution using conc. HCl until pH of around 1 was obtained. The product was filtered by vacuum filtration and dried overnight to obtain pale white yellow powder.

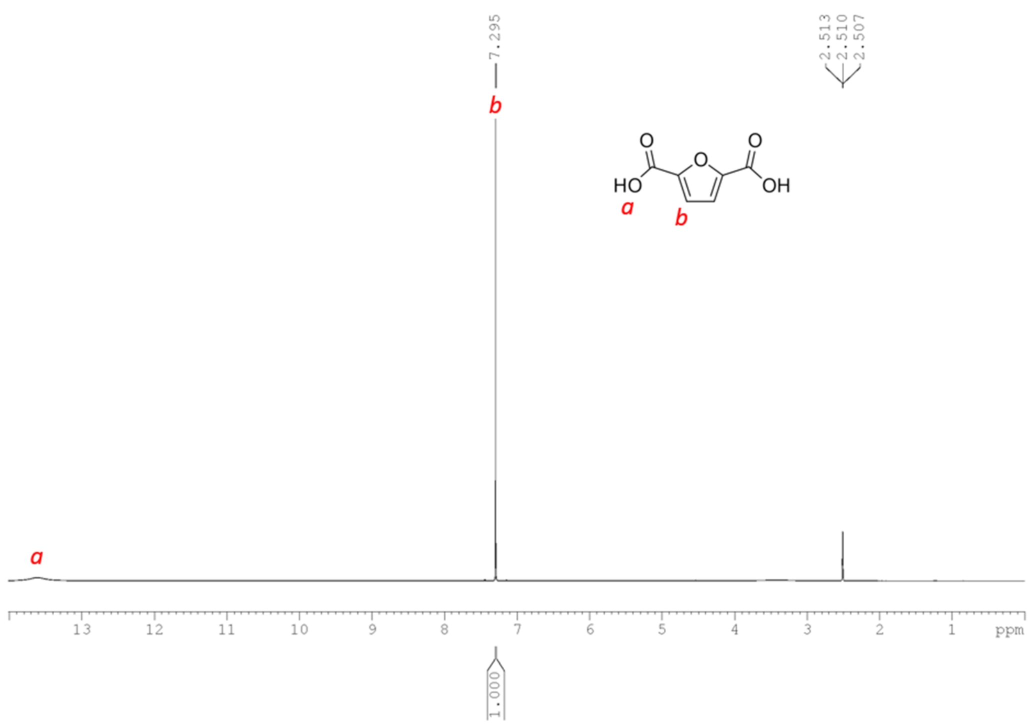

Figure S17. ^{1}H NMR of FDCA.

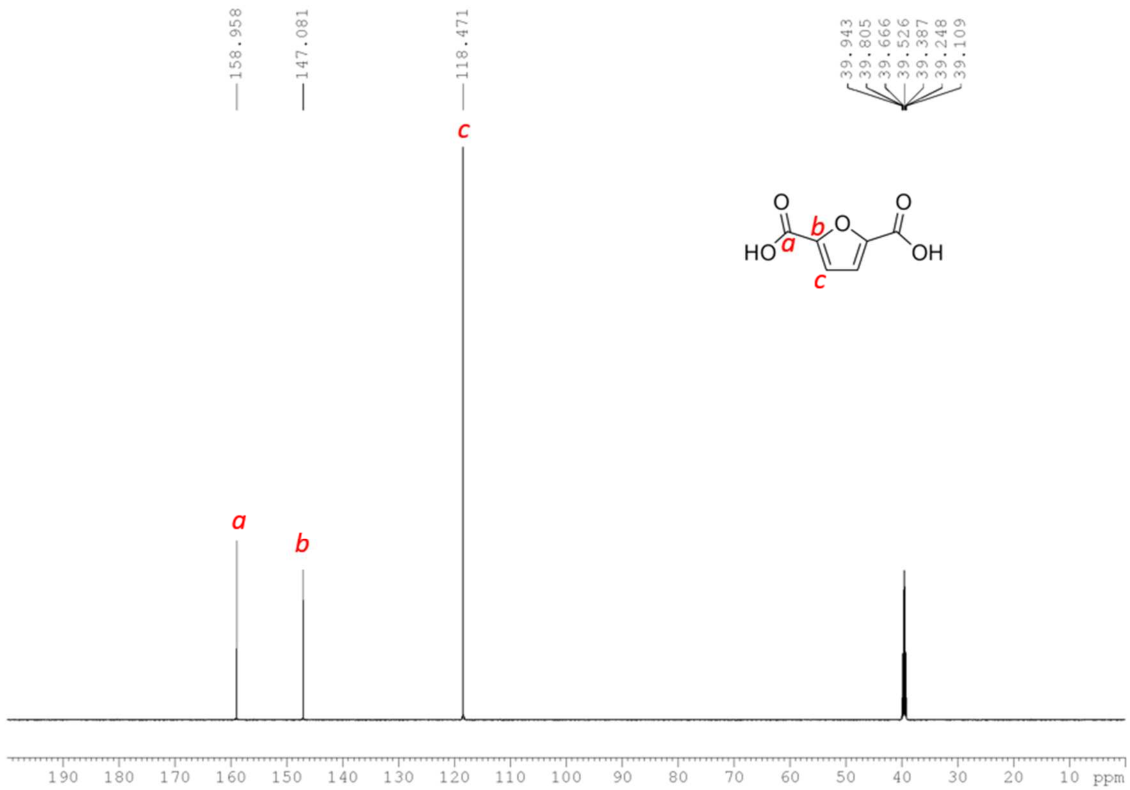

Figure S18. ^{13}C NMR of FDCA.

References

1. J. Ren, K.-h. Song, Z. Li, Q. Wang, J. Li, Y. Wang, D. Li and C. K. Kim, *Appl. Surf. Sci.*, 2018, ***456***, 174-183.

2. X. Liao, J. Hou, Y. Wang, H. Zhang, Y. Sun, X. Li, S. Tang, K. Kato, M. Yamauchi and Z. Jiang, *Green Chem.*, 2019, **21**, 4194-4203.

3. G. Henkelman, A. Arnaldsson and H. Jónsson, *Comput. Mater. Sci.*, 2006, **36**, 354-360.

4. E. Hayashi, Y. Yamaguchi, K. Kamata, N. Tsunoda, Y. Kumagai, F. Oba and M. Hara, *J. Am. Chem. Soc.*, 2019, **141**, 890-900.

5. K. Gupta, R. K. Rai and S. K. Singh, *Inorg. Chem. Front.*, 2017, **4**, 871-880.